Research Article | Vol. 24, No. 22 | 31 Oct 2016 | OPTICS EXPRESS 25103

Optics EXPRESS

Silicon-based multilayer gratings with a designable narrowband absorption in the short-wave infrared

XIAOYI LIU,[1,2] JINSONG GAO,[1,2,3] HAIGUI YANG,[1,4] XIAOYI WANG,[1] AND JINGLI ZHAO[1]

[1]*Key Laboratory of Optical System Advanced Manufacturing Technology, Changchun Institute of Optics, Fine Mechanics and Physics, Chinese Academy of Sciences, Changchun 130033, China*
[2]*University of the Chinese Academy of Sciences, Beijing 100039, China*
[3]*gaojs999@163.com*
[4]*yanghg@ciomp.ac.cn*

Abstract: We demonstrate an Al/Si multilayer-grating microstructure covered on Si substrate. This microstructure presents a designable narrowband absorption in short-wave infrared (SWIR) waveband (2.0 μm-2.3 μm). We investigate its absorption mechanism by both modeling and simulations, and explain the results well with metal-insulator-metal and Fabry-Perot cavity theory. Furthermore, we present the absorption of fabricated multilayer-grating microstructure through experiment, and discuss the influence of structure's lateral angle on its absorption in detail. This work provides the possibility to design Si-based devices with designable working bands in SWIR spectrum.

OCIS codes: (040.6040) Silicon; (240.6680) Surface plasmons; (250.5403) Plasmonics.

References and links

1. T. K. Liang and H. K. Tsang, "Efficient Raman amplification in silicon-on-insulator waveguides," Appl. Phys. Lett. **85**(16), 3343–3345 (2004).
2. A. Liu, H. Rong, M. Paniccia, O. Cohen, and D. Hak, "Net optical gain in a low loss silicon-on-insulator waveguide by stimulated Raman scattering," Opt. Express **12**(18), 4261–4268 (2004).
3. S. Manipatruni, Q. Xu, and M. Lipson, "PINIP based high-speed high-extinction ratio micron-size silicon electrooptic modulator," Opt. Express **15**(20), 13035–13042 (2007).
4. P. Zhang, S. Li, C. Liu, X. Wei, Z. Wu, Y. Jiang, and Z. Chen, "Near-infrared optical absorption enhanced in black silicon via Ag nanoparticle-induced localized surface plasmon," Nanoscale Res. Lett. **9**(1), 519 (2014).
5. Y. Wang, J. Gao, H. Yang, X. Wang, and Z. Shen, "Compensating the degradation of near-Infrared absorption of black silicon caused by thermal annealing," Nanoscale Res. Lett. **11**(1), 56 (2016).
6. M. W. Knight, H. Sobhani, P. Nordlander, and N. J. Halas, "Photodetection with active optical antennas," Science **332**(6030), 702–704 (2011).
7. M. A. Nazirzadeh, F. B. Atar, B. B. Turgut, and A. K. Okyay, "Random sized plasmonic nanoantennas on Silicon for low-cost broad-band near-infrared photodetection," Sci. Rep. **4**, 7103 (2014).
8. W. Li and J. Valentine, "Metamaterial perfect absorber based hot electron photodetection," Nano Lett. **14**(6), 3510–3514 (2014).
9. C. F. Guo, T. Y. Sun, F. Cao, Q. Liu, and Z. F. Ren, "Metallic nanostructures for light trapping in energy-harvesting devices," Light Sci. Appl. **3**(4), e161 (2014).
10. Q. Min and R. Gordon, "Surface plasmon microcavity for resonant transmission through a slit in a gold film," Opt. Express **16**(13), 9708–9713 (2008).
11. K. Wu, T. Rindzevicius, M. S. Schmidt, K. B. Mogensen, S. Xiao, and A. Boisen, "Plasmon resonances of Ag capped Si nanopillars fabricated using mask-less lithography," Opt. Express **23**(10), 12965–12978 (2015).
12. Y. Zhu, X. Hu, H. Yang, and Q. Gong, "On-chip plasmon-induced transparency based on plasmonic coupled nanocavities," Sci. Rep. **4**, 3752 (2014).
13. D. K. Gramotnev and S. I. Bozhevolnyi, "Nanofocusing of electromagnetic radiation," Nat. Photonics **8**(1), 13–22 (2013).
14. S. I. Bozhevolnyi, V. S. Volkov, E. Devaux, J. Y. Laluet, and T. W. Ebbesen, "Channel plasmon subwavelength waveguide components including interferometers and ring resonators," Nature **440**(7083), 508–511 (2006).
15. D. M. Koller, A. Hohenau, H. Ditlbacher, N. Galler, F. Reil, F. R. Aussenegg, A. Leitner, E. J. W. List, and J. R. Krenn, "Organic plasmon-emitting diode," Nat. Photonics **2**(11), 684–687 (2008).
16. R. J. Walters, R. V. A. van Loon, I. Brunets, J. Schmitz, and A. Polman, "A silicon-based electrical source of surface plasmon polaritons," Nat. Mater. **9**(1), 21–25 (2010).

#274583 http://dx.doi.org/10.1364/OE.24.025103
Journal © 2016 Received 29 Aug 2016; revised 14 Oct 2016; accepted 14 Oct 2016; published 18 Oct 2016

Optics EXPRESS

17. K. Ding and C. Z. Ning, "Metallic subwavelength-cavity semiconductor nanolasers," Light Sci. Appl. **1**(7), e20 (2012).
18. Y. J. Lu, C. Y. Wang, J. Kim, H. Y. Chen, M. Y. Lu, Y. C. Chen, W. H. Chang, L. J. Chen, M. I. Stockman, C. K. Shih, and S. Gwo, "All-color plasmonic nanolasers with ultralow thresholds: autotuning mechanism for single-mode lasing," Nano Lett. **14**(8), 4381–4388 (2014).
19. K. T. Lin, H. L. Chen, Y. S. Lai, and C. C. Yu, "Silicon-based broadband antenna for high responsivity and polarization-insensitive photodetection at telecommunication wavelengths," Nat. Commun. **5**, 3288 (2014).
20. X. Y. Liu, J. S. Gao, H. G. Yang, H. Liu, X. Y. Wang, and Z. F. Shen, "Near-infrared absorption enhancement mechanism investigations of deep-trench silicon microstructures covered with gold films," Plasmonics **11**(4), 1019–1024 (2016).
21. Y. J. Liang, F. Liu, Y. F. Chen, X. J. Wang, K. N. Sun, and Z. W. Pan, "New function of the Yb^{3+} ion as an efficient emitter of persistent luminescence in the short-wave infrared," Light Sci. Appl. **5**(7), e16124 (2016).
22. C. Mermelstein, S. Simanowski, M. Mayer, R. Kiefer, J. Schmitz, M. Walther, and J. Wagner, "Room-temperature low-threshold low-loss continuous-wave operation of 2.26 μm GaInAsSb/AlGaAsSb quantum-well laser diodes," Appl. Phys. Lett. **77**(11), 1581–1583 (2000).
23. A. Sobhani, M. W. Knight, Y. Wang, B. Zheng, N. S. King, L. V. Brown, Z. Fang, P. Nordlander, and N. J. Halas, "Narrowband photodetection in the near-infrared with a plasmon-induced hot electron device," Nat. Commun. **4**, 1643 (2013).
24. M. W. Knight, Y. Wang, A. S. Urban, A. Sobhani, B. Y. Zheng, P. Nordlander, and N. J. Halas, "Embedding plasmonic nanostructure diodes enhances hot electron emission," Nano Lett. **13**(4), 1687–1692 (2013).
25. F. Hu, H. Yi, and Z. Zhou, "Band-pass plasmonic slot filter with band selection and spectrally splitting capabilities," Opt. Express **19**(6), 4848–4855 (2011).
26. M. Bora, E. M. Behymer, D. A. Dehlinger, J. A. Britten, C. C. Larson, A. S. P. Chang, K. Munechika, H. T. Nguyen, and T. C. Bond, "Plasmonic black metals in resonant nanocavities," Appl. Phys. Lett. **102**(25), 251105 (2013).
27. J. Petschulat, C. Helgert, M. Steinert, N. Bergner, C. Rockstuhl, F. Lederer, T. Pertsch, A. Tünnermann, and E. B. Kley, "Plasmonic modes of extreme subwavelength nanocavities," Opt. Lett. **35**(16), 2693–2695 (2010).

1. Introduction

Silicon, one of the most abundant elements in earth's crust, has a lot of excellent properties: It possesses significant nonlinearity, resulting in an easily achievement of optical amplification or stimulated Raman scattering [1,2], ect.; Its remarkable plasma dispersion effect is widely applied into optical modulation technology [3]. Furthermore, due to the large intrinstic bandgap (1.12eV), it is practically transparent in near infrared (NIR)/short-wave infrared (SWIR) waveband. Accordingly, Si can be referred as a good candidate of waveguide in NIR/SWIR band. However, just because of lacking absorption, Si material is not applicable for fabricating NIR/SWIR receiver and detector [4,5], which can only be substituted by Ge or InGaAs currently. It brings about a large difficulty in the integration of on-chip devices, consequently limiting the application range of Si devices. So developing NIR/SWIR Si-based detector has become one of the hotspots of silicon photonics [6–8].

Surface plasmon polariton (SPP), a surface wave that propagates along the interface between metal and insulator, can confine the energy into a very thin area effectively [9–12]. It also has a relatively long wave vector that provides the possibility of breaking diffraction limit [13]. On this account, SPP is widely used in optical resonator, emitter and spacer techniques [14–18]. In addition, SPP will make the Schottky barrier at the metal-Si interface replace Si bandgap to become its limitation of absorption spectrum [19,20]. In other words, it offers a new approach to extend Si absorption band and prepare Si-based NIR/SWIR detector.

According to the contents above, we demonstrate a microstructure of multiple grating that alternate Al and Si layers are utilized to instead of typical single material grating stripes. Not only SPPs can be excited by the grating-shaped structure, but the multiple layers in stripes can form Fabry-Perot (F-P) cavities, by which we can achieve a designable narrowband absorption in SWIR range (2.0 μm-2.3 μm), corresponding to the major working bands of various advanced devices such as trivalent ytterbium (Yb^{3+}) ion emitter or quantum well laser [21,22], and the SWIR atmospheric window includes this band as well. Detailed discussion and investigation are given below.

Optics EXPRESS

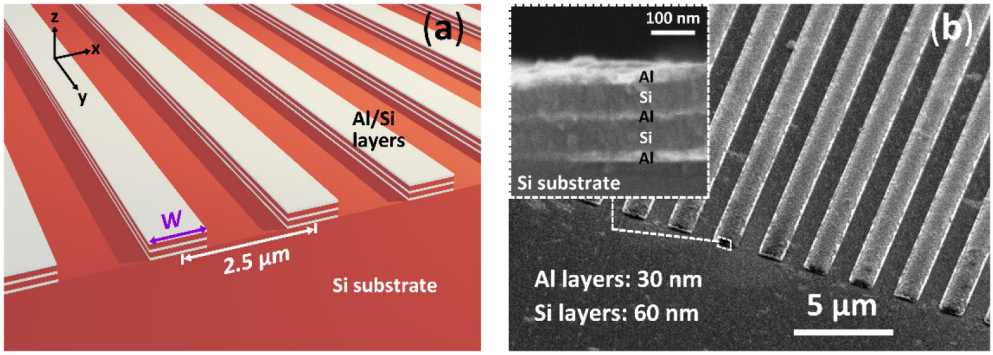

Fig. 1. (a) Diagram of the designed multilayer-grating microstructure. (b) Top-view SEM image of fabricated multilayer-grating microstructure. The inset shows the cross-sectional SEM image of alternate Al and Si layers.

2. Experiment and simulation modeling

A diagram of the multilayer grating is shown in Fig. 1(a) to illustrate its structure. The grating stripe is consisted of five alternant layers covering on Si substrate, containing three 30 nm-thick Al layers and two 60 nm-thick Si layers, with a grating constant of 2.5 μm. These structural parameters will be carefully discussed in the next section. It is prepared by the following process. After chemical cleaning of surface native oxide in hydrogen fluoride and acetone solutions, we deposited a 300 nm-thick photoresist on Si substrate by spin coating, and subsequently patterned using laser direct writing method. Then the sample is developed for 30 s in NaOH solutions. Next, it is immediately transferred into a magnetron sputtering machine to deposit Al and Si layers successively. After that, we soaked the sample in acetone solutions to dissolve the left photoresist, leading to the formation of grating structure. Figure 1(b) shows the top-view SEM image of fabricated multilayer-grating microstructure, in which the cross-sectional SEM image of alternate Al and Si layers is also presented.

On the other hand, we use finite difference-time domain (FDTD) method to investigate the characteristics of designed multilayer grating. In our simulations, we adopt an x-polarized plane wave as the normal incidence source, and set periodic condition as the boundary condition in x- and y-directions. In z-direction we use perfectly matched layer (PML) condition for the sake of measuring transmittance (T) and reflectance (R), and extracting absorptance (A) as $A = 1\text{-}T\text{-}R$. Meanwhile, we also adopt a high mesh accuracy (3 nm) to guarantee the convergence of simulations, and a series of repeated simulations to verify its stability. All the aspects mentioned above should be paid attention to in modeling; otherwise the reliability of following calculations will not be ensured.

3. Results and discussions

Firstly, Fig. 2(a) illustrates the dependence of simulated absorption curves on the stripe width (W) of multilayer-grating microstructures. Increasing W from 1.15 μm to 1.35 μm tunes absorption peak wavelength from 1.99 μm to 2.30 μm, precisely in the SWIR atmospheric window. This calculation brings about a crucial significance that the narrowband absorption peak of designed multilayer grating can be tuned by controlling W in the focused SWIR working band. It will provide conveniences for realizing a Si-based SWIR response band device. The redshift phenomenon satisfies the general rule of grating-shaped microstructure [23,24]; however, its mechanism should be discussed thoroughly.

Optics EXPRESS

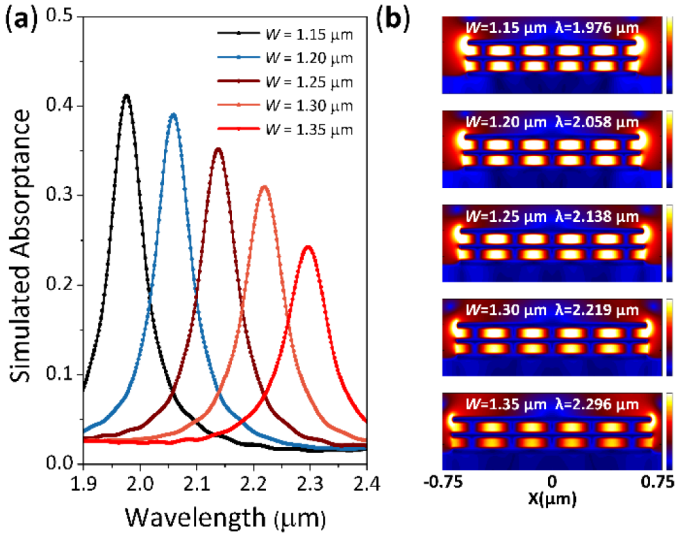

Fig. 2. (a) The dependence of simulated absorptance on the W of the multilayer-grating microstructures. (b) Longitudinal (xz-plane) electric-field intensity distributions of the microstructures with different W from 1.15 μm to 1.35 μm. The colorbars stand for the normalized electric field intensity.

Figure 2(b) displays the longitudinal electric-field intensity distributions of the microstructure with different W from 1.15 μm to 1.35 μm. The incident light wavelengths respectively correspond to their peak wavelengths in the absorption curves of Fig. 2(a). Proverbially, by the grating-shaped structure, SPPs will be excited at Al-Si interfaces, and their penetration depths on Al side are much smaller than that on Si side, resulting in confining energies in Si layers. Meanwhile, SPPs propagating along Si layers form standing waves between two Si-air interfaces, so the energy has transverse nodal arrangement mode that composed by bright and dark regions alternately. To be more specific, two Si-air interfaces and the Si layer inside form a transverse F-P cavity, which induces a nodal energy distribution mode at the resonance wavelength.

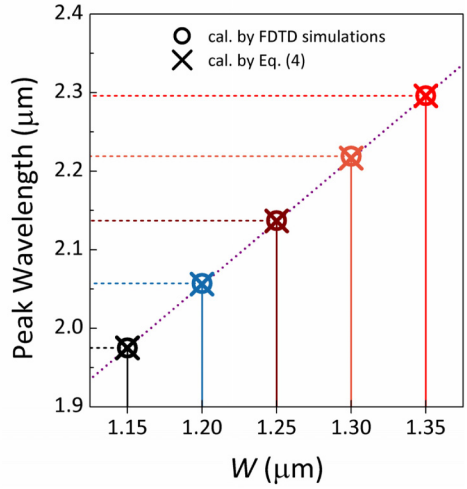

Fig. 3. The relationship between W and absorption peak wavelength of the microstructures calculated by Eq. (4) and FDTD simulations, respectively.

Optics EXPRESS

Accordingly, the transverse F-P cavity sandwiched in metal-insulator-metal (MIM) structure is the core of our designed multilayers grating, so we can make some mathematical descriptions with MIM and cavity theory. First of all, we can give the resonance condition generally for these waveguides as [25,26]:

$$2W\beta + \varphi_r = 2m\pi \tag{1}$$

where β is complex propagation constant, and m is the resonance order. φ_r is the phase shift of propagating waves at two facets of the waveguide, and W is the width of grating stripe, which represents the length of F-P cavity. So we can write the expression of m as follows:

$$m = (2W\beta + \varphi_r)/2\pi \tag{2}$$

it means we can figure out resonance order m only requiring the value of β. Fortunately, on the basis of waveguide theory, the complex propagation constant β can be figured out by solving following dispersion equations [25,27]:

$$\begin{aligned} \varepsilon_d k_m + \varepsilon_m k_d \tanh(k_d h/2) = 0 \\ \beta^2 - \varepsilon_d k_0^2 = k_d^2 \\ \beta^2 - \varepsilon_m k_0^2 = k_m^2 \end{aligned} \tag{3}$$

where ε_d and ε_m are dielectric constants of Si and Al respectively, and h is the thickness of Si layers (60 nm). $k_0 = 2\pi/\lambda$ is the free space wave vector. Following the steps mentioned in Eqs. (1)-(3), we can obtain the values of β, and confirm the resonance order m (m = 3). Additionally, in order to forecast the resoncance wavelength λ_r by the mathematical model above, we introduce the concept of effective refractive index n_{eff} of the MIM waveguide as $n_{eff} = \beta/k_0$ [25]. According to it, we express the resonance wavelength λ_r as follows:

$$\lambda_r = 2n_{eff}W/(m - \varphi_r/2\pi) \tag{4}$$

therefore, λ_r can be easily obtained as long as we substitute n_{eff} and m into this equation. What's more, we can use it to provide a quantitative comparison with the results of FDTD simulations. It should be noted that the phase shift term $\varphi_r/2\pi$ locates in the denominator of Eq. (4), leading to a great influence on λ_r, so it cannot be treated as a constant for different W. In practical computations, we firstly get the values of $\varphi_r/2\pi$ when W = 1.15 μm (0.876) and W = 1.35 μm (0.850) from equations above. Based on them, we obtain other phase shift values by a linear fitting, and subsequently figure out all the resonance wavelengths λ_r to contrast with simulations. Figure 3 shows the relationship between W and absorption peak wavelengths calculated by FDTD simulations and Eq. (4) respectively. We can see that the results deduced by Eq. (4) are coincident with that by FDTD simulations very well, and the small deviations could be induced by the inappropriate fitting method for the phase shift. Clearly the resonance wavelength λ_r is proportional to the width of grating stripe W, which is intelligible that it can be observed by Eq. (4) directly. Naturally, the redshift phenomenon in Fig. 2(a) can also be explained by this equation. In Fig. 2(b), although the models have different W in simulations, they have the same resonance order, causing a similar electric-field intensity distribution mode. It is a typical F-P cavity system with a frequency-sensitive characteristic that only the frequency-matched SPPs can produce standing waves by coherent superposition, which can explain the narrowband absorption peaks in Fig. 2(a).

We further investigate the dependence of simulated absorption peak value on the layer number and layer thickness of the multilayer-grating microstructure, as shown in Figs. 4(a) and 4(b), respectively. It can be seen that with the layer number or thickness increase, the absorptance tends to be saturated. Considering the deep trench often brings about problems on fabrication process, as mentioned before, we adopt a relatively few layer number (five layers)

Optics EXPRESS

and thin thickness (Al: 30 nm, Si: 60 nm) in experiments, thereby endeavoring to guarantee the profile quality of designed multilayer grating.

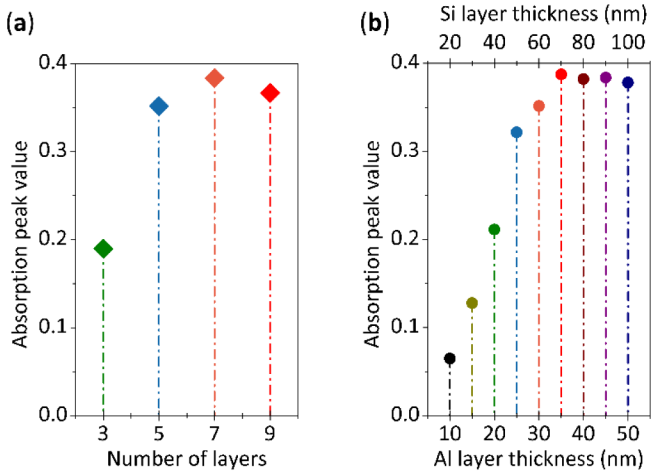

Fig. 4. (a) The dependence of simulated absorption peak value on the number of stacked layers of designed multilayer grating. (b) The dependence of simulated absorption peak value on layer thickness of designed multilayer grating.

Figure 5(a) shows the experimental absorption curve with W = 1.25 μm. For comparison, we also give the simulated absorption curve. The experimental displays the similar absorption as the simulated, and they almost have the same peak value. It gives a strong support to the reliability of the theoretical analysis in this study. However, by a careful comparison, we can find that the experimental absorption peak is relatively wider, and its peak wavelength has a small deviation from simulated one. This is actually because that the fabricated microstructures in experiment distinguish from the designed in Fig. 1(a). Figures 5(b) and 5(c) show two representative cross-sectional SEM images of a fabricated multilayer grating. Obviously, the fabricated grating has oblique lateral angles (θ) due to our fabrication technique limitation. While our theoretical analysis is based on a perfect grating microstructure with $\theta = 90°$.

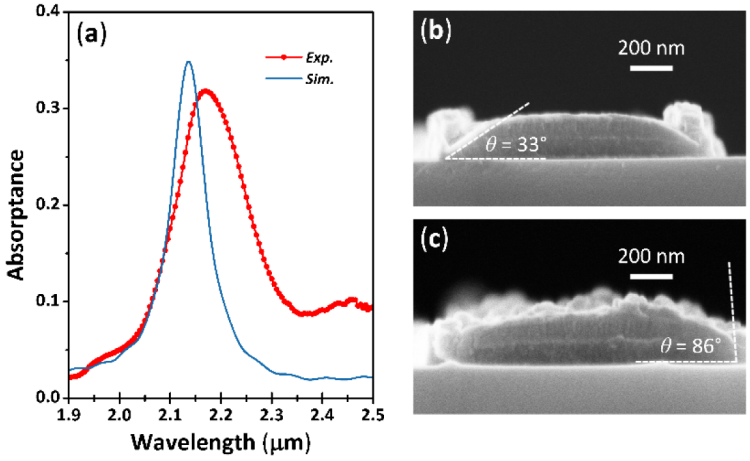

Fig. 5. (a) The experimental absorptance (red) and simulated absorptance (blue) of the multilayer-grating microstructure with W = 1.25 μm. (b) Cross-sectional SEM image of prepared microstructure with lateral angle $\theta = 33°$. (c) Cross-sectional SEM image of prepared microstructure with lateral angle $\theta = 86°$.

Optics EXPRESS

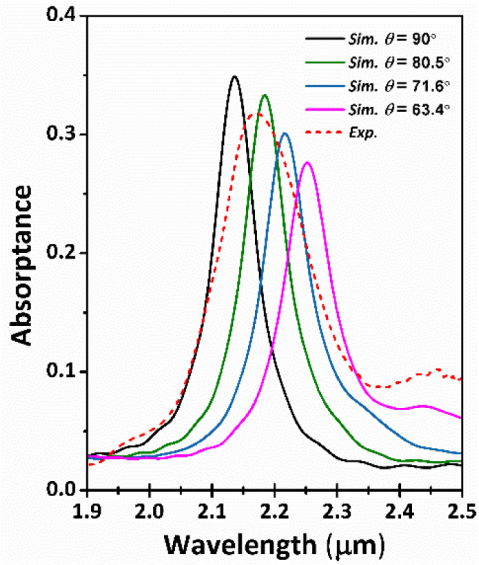

Fig. 6. The relationship between simulated absorptance and the lateral angle (θ) of the multilayer-grating microstructures. The experimental value is also given (dashed line).

In order to explain the difference between the experimental and simulated absorption originated from oblique lateral angles, we build several models with different θ in simulations, and compare their absorption. From Fig. 6 we can know that decreasing the angle will make the absorption peak wavelength gradually deviate from its original position. It is understandable that oblique lateral sidewalls represent unequal lengths of F-P cavities in the grating stripes, consequently making they have slightly different resonance wavelengths. As a result, the resonance wavelength exhibits a red-shift behavior with θ decrease. For the fabricated microstructures as shown in Figs. 5(b) and 5(c), they have a θ with a wide variation range, therefore the experimental result displays a broader absorption peak. It can be seen from Fig. 6 that the experimental data (dashed line) is much closer to the simulated results contained different lateral angles of gratings. Moreover, it is noted that due to the good ductility of Al material, there still have some residuals near both sides of each grating stripes after soaking samples by acetone solutions (see Figs. 5(b) and 5(c)), which may also interfere the experimental results slightly.

Finally, we have mentioned the concept of resonance order m in the content about quantitative analysis by equations. It implies that for a certain cavity length there may exist more than one resonance wavelengths [26]. By simulations, Fig. 7 summarizes the absorptance of our microstructures with various W from 1.0 μm to 1.7 μm, and the spectrum range is from 1.3 μm to 2.5 μm. It can be seen that evidently it expresses the linear redshift phenomenon of absorption peak with W increasing. More importantly, some higher order resonance modes exactly appear in relatively shorter waveband. Actually we have observed the higher order resonance peak at 1.5 μm except the peak at 2.2 μm for W = 1.25 μm in experiments. We can find at least one resonance mode of narrowband absorption at every commonly used SWIR wavelengths. As is known, the SWIR atmospheric window is mainly composed of two wavebands (1.4 μm - 1.9 μm, 2.0 μm - 2.5 μm, respectively). Therefore, the designed multilayer grating even more actualizes the possibility of multiple SWIR bands, or dual major SWIR atmospheric windows response. In addition, we can shift its response bands to our interested ranges through changing the width W of grating stripes, which offers a new perspective to accomplish controlling and regulating devices' working bands in the whole SWIR spectrum.

Optics EXPRESS

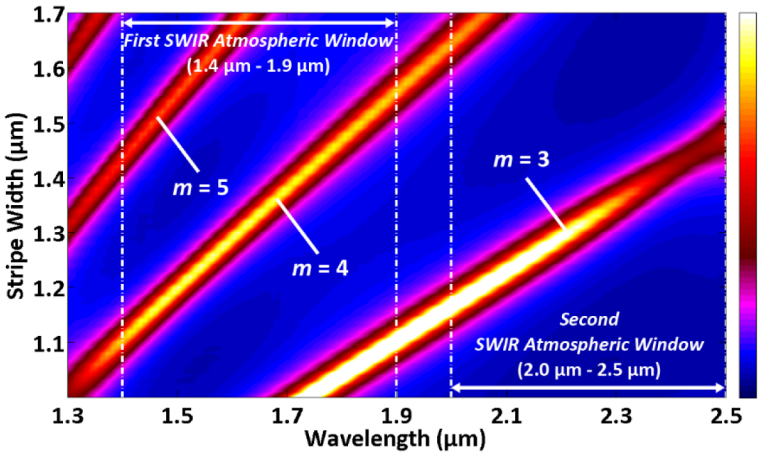

Fig. 7. Summary of the absorption spectrum of multilayer-grating microstructures with various stripe width (*W*). The colorbar stands for the relative absorptance.

4. Conclusion

In summary, we successfully demonstrate a designable SWIR narrowband absorption by using an Al/Si multilayer-grating microstructure covered on Si substrate. Its SWIR absorption band is designable from 2.0 μm to 2.3 μm for the different widths of grating stripes. The absorption peak wavelengths of the grating-shaped structure are deduced by MIM waveguide and F-P cavity theory quantitatively, which agree very well with the results of FDTD simulations. We observe that the energy is highly localized in Si layers, which forms a transverse F-P cavity along with the neighbor Al layers, and induces a nodal energy distribution mode inside at the resonance wavelength. Furthermore, we find that decreasing lateral angles of our microstructure shifts its resonance wavelength slightly, resulting in a broader absorption peak in experiment. It is expected that the designed multilayer-grating microstructure covered on Si substrate offers a great significance for Si-based SWIR devices.

Funding

This project was supported by the National Natural Science Foundation of China (Nos. U1435210, 61306125, 61675199 and 11604329), the Science and Technology Innovation Project (Y3CX1SS143) of CIOMP, the Science and Technology Innovation Project of Jilin Province (Nos. 20130522147JH and 20140101176JC).